Nanostructures

DOI: 10.1002/anie.201005493

Superstructures and SERS Properties of Gold Nanocrystals with Different Shapes**

Zhening Zhu, Haifeng Meng, Wenjing Liu, Xinfeng Liu, Jianxiao Gong, Xiaohui Qiu, Lei Jiang, Dan Wang, and Zhiyong Tang**

Inorganic nanocrystal (NC) superstructures, which exhibit unique collective properties that are different to those of both the individual NCs and bulk materials, are of much scientific and technological interest.[1–5] For noble-metal NCs, the collective oscillation of free electrons, that is, the so-called plasmon resonance in the superstructures, provides a feasible way to realize light concentration and manipulation on a small scale.[6] Such plasmon resonance gives rise to many potential applications of noble-metal NC superstructures in different fields, for example, optical waveguides,[7] superlensing,[8] photon detection,[9] and surface-enhanced Raman scattering (SERS). Among these applications, the SERS effect based on noble-metal NC superstructures is of particular interest because of its extraordinary advantages in the highly sensitive detection of trace chemical or biological species.[10,11]

The SERS effect originates from the dramatic amplification of electromagnetic fields in the NC superstructures. When the superstructures are irradiated at the wavelength that couples with the plasmon resonance of the inner NCs, the junction regions among the adjacent NCs function as "hotspots" and the local electromagnetic fields in the superstructure are amplified.[12] As a result, the Raman scattering of the detected species located at these junctions will be remarkably enhanced. Evidently, the intensity of SERS in the superstructures is determined not only by the type, shape, and size of the single NC units, but also by the inter-NC distance and arrangement pattern. Although many reports have shown that the 1D, 2D, and 3D assemblies of noble-metal NCs can be used as efficient substrates for SERS,[13] the corresponding studies on the NC superstructures are rare because of the difficulties in synthesis of monodispersed NCs that have different shapes, as well as the controlled organization of NCs on a large scale. In order to understand and maximize the SERS effect, large-scale NC superstructures with controllable morphologies are highly desirable. Herein we report how three types of Au NCs with identical sizes but different shapes can be used as building blocks to prepare superstructures on several different substrates. We demonstrate that both the structures and morphologies of the superstructures are highly dependent on the shapes of the NC units, and furthermore, that these superstructures exhibit obvious differences in their SERS properties. Both the formation mechanism and the SERS properties of the different Au NC superstructures are explored in detail.

The seed-mediated growth method was used to synthesize single-crystalline rhombic dodecahedral (RD), octahedral, and cubic Au NCs by manipulating the growth kinetics of the NCs (see the Experimental Section). As reported in our previous study, RD, octahedral, and cubic Au NCs are bounded by twelve (110) planes, eight (111) planes, and six (100) planes, respectively.[14] The three types of Au NCs, with an average size of around 70 nm, have well-defined shapes and good monodispersity (Figure S1 in the Supporting Information). Such Au NCs with highly uniform sizes and shapes guarantee the reproducibility of subsequent self-assembly processes.

2D and 3D superstructures of Au NCs were fabricated by a vertical deposition self-assembly method,[15] which is a conventional technique for the formation of photonic crystals that are composed of colloidal particles (see the Experimental Section).[16,17] Interestingly, when the concentration of the NCs is fixed at 0.5 nM, most of the RD NCs (more than 99%) are spontaneously and closely packed into well-defined multilayers of face-centered-cubic (fcc) structures on silicon substrates (Figure 1); each layer is a triangle and the edge length of each layer gradually decreases as the thickness increases (Figure 1b). Generally, the sizes of the 3D triangular superstructures vary from 1 μm to 6 μm, and each RD NC in every superstructure has the same spatial orientation with a threefold symmetry axis vertical to the substrate (Figure 1c,d). Therefore, the RD NCs tend to assemble into a close-packed fcc superstructure, in which each RD NC in the

[*] Z. Zhu, W. Liu, X. Liu, J. Gong, Prof. X. Qiu, Prof. Z. Tang
National Center for Nanoscience and Technology
Beijing 100190 (P.R. China)
Fax: (+86) 10-6265-6765
E-mail: zytang@nanoctr.cn
Prof. D. Wang
State Key Laboratory of Multi-phase Complex Systems
Institute of Process Engineering
Chinese Academy of Sciences, Beijing 100190 (P.R. China)
E-mail: danwang@home.ipe.ac.cn
Prof. L. Jiang
Institute of Chemistry, Chinese Academy of Sciences
Beijing 100190 (P.R. China)
Dr. H. Meng
National Institute of Metrology, Beijing 100013 (P.R. China)

[**] This work was supported by the National Natural Science Foundation for Distinguished Youth Scholars of China (21025310, Z.Y.T), the National Research Fund for Fundamental Key Project (2009CB930401), the 100-Talent Program of the Chinese Academy of Sciences, and the National Science Foundation of China (20973047). We also thank Prof. Hongxing Xu at the Institute of Physics, Chinese Academy of Sciences for his help with the characterization of optical properties of NC superstructures.
SERS = surface-enhanced Raman scattering.

Supporting information for this article is available on the WWW under http://dx.doi.org/10.1002/anie.201005493.

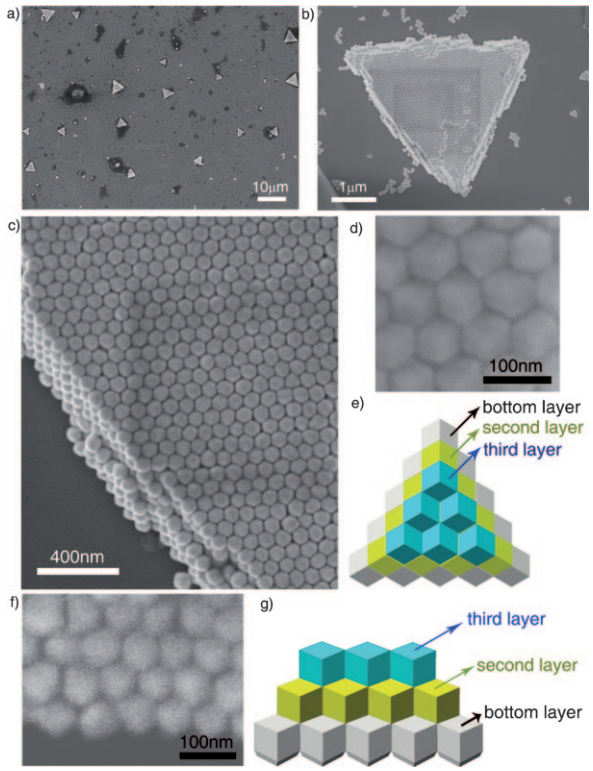

Figure 1. SEM and schematic images of self-assembled RD Au NCs on silicon substrates. a) Full SEM image showing many triangular superstructures; b) single triangular superstructure; c) magnified image of a triangular superstructure; d) arrangement of Au NCs (top view); e) top view of the self-assembly pattern showing three different layers in the fcc close-packed arrays; f) side view of the superstructure when tilting the sample stage by 60°; g) side view of the self-assembly pattern showing that the RD NCs in the bottom layer are in contact with the substrate through one vertex.

medium layers is surrounded by twelve adjacent RD NCs through (110) plane contacting (six NCs are located in the same layer, and the adjacent upper and lower layers each contain three NCs); one vertex of the RD NCs in the bottom layer are in contact with the substrate (Figure 1 f, g and Figure S2 in the Supporting Information). AFM characterization further confirms the close-packed pattern of the RD NC superstructures (see Figure S3 in the Supporting Information). For comparison, the assembly behavior of octahedral and cubic Au NCs (both 0.5 nM) are different and a 2D monolayer is formed in which one plane is in direct contact with the silicon substrates (Figure 2 a, b). As a result, the vertices of octahedral NCs point to the face centers of the adjacent NCs within the monolayer (Figure 2 c), while the cubic NCs are close-packed through face–face interactions (Figure 2 d). When the concentration of the NCs is increased to approximately 5 nM, both octahedral and cubic Au NCs assemble into multilayered superstructures without well-defined profiles (Figure S4 and S5 in the Supporting Information), and the arrangements of NCs in the 3D superstructures are similar to those in the 2D monolayer.

The two main reasons for the self-assembly of different concentrations of differently shaped Au NCs into superstructures with different structures and morphologies are the

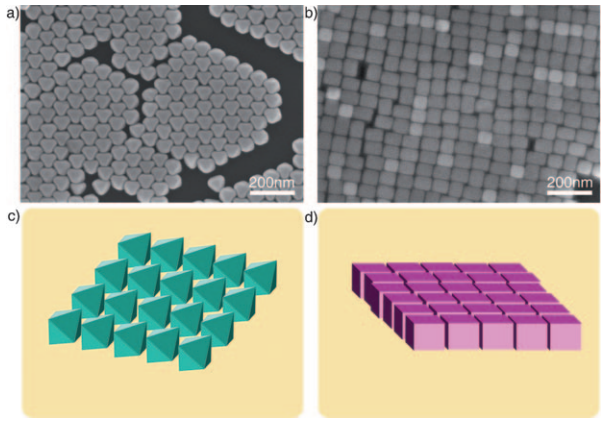

Figure 2. SEM and schematic images of superstructures self-assembled by octahedral and cubic Au NCs. a) Octahedral Au NCs; b) cubic Au NCs; self-assembly behavior for c) octahedral and d) cubic Au NCs.

critical concentration of the Au NCs and the inter-NC van der Waals interactions. The formation of the superstructures is highly dependent on the critical concentration of the Au NCs (Scheme S1 in the Supporting Information). As the solvent evaporates, the Au NCs reach a critical concentration, self-assemble on the three-phase-contact line (the interface of vapor, substrate, and Au NCs solution), and finally form superstructures. When the RD Au NCs are at a low supersaturated concentration, contact with the substrate through one plane is the most stable way of deposition (Figure 3 b, d). However, as the concentration of the NCs increases, the RD Au NCs spontaneously change their adsorption pattern from lying (contact with substrate through one plane) to standing (contact with the substrate through one vertex), and form the multilayered structures. In these structures, RD NCs are in contact with the adjacent 12 NCs through face–face contacts, and thus maximize the inter-NC Van der Waals force interactions (Figure 1 c–g). Compared with the RD NCs monolayer that contains single-face contacts, the inter-NC attractions in the multilayer are remarkably high, which is sufficiently large to compensate for the energy required for the configuration changes (from lying to standing) of NCs in the bottom layer of the superstructures. On the contrary, such

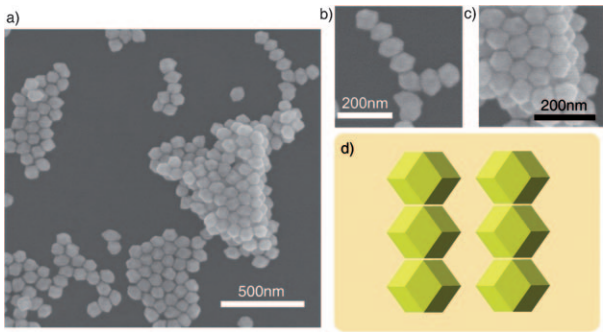

Figure 3. Intermediate state of RD Au NCs on the silicon substrate during the self-assembly process. a) Full SEM image; b) RD NCs that contact the substrates with one plane at low concentrations; c) change in the assembly pattern of the RD NCs in the multilayered superstructures; d) schematic image of the RD NCs lying on the substrate at low concentrations.

a change of arrangement methods is not energetically favorable for both cubic and octahedral NCs. For example, cubic NCs in the monolayer have four faces that are in contact with adjacent NCs and one face that lies on the substrates (Figure 2b,d), which is quite a stable state. No extra face–face interaction can be obtained for the octahedral NCs, even if the adsorption pattern on the substrates changes from lying to standing. Therefore, both cubic and octahedral NCs tend to assemble into 2D monolayers at relatively low concentrations (0.5 nM). As the concentration of the NC solution increases (to 5 nM), the number of NCs per unit volume also greatly increases and easily results in formation of the multilayered superstructure of cubic and octahedral Au NCs (Figures S4 and S5 in the Supporting Information). RD Au NCs in the triangular superstructures organize into an fcc lattice with a packing density of almost 100% in Euclidean 3D space; this arrangement is believed to be the densest possible packing of equal spheres in ordinary space.[18] We have also observed that the arrangement of NCs in the superstructures is mainly dependent on the interactions between NCs rather than the properties of the substrates. This observation is confirmed by self-assembly experiments of different shaped Au NCs on glass substrates, and three similar types of superstructures are observed (Figure S6 in the Supporting Information).

Interestingly, the superstructures fabricated from different shaped Au NCs exhibit different collective optical properties and unique SERS effects. *p*-Mercaptoaniline (*p*MA), which is a nonresonant molecule, is used as the model analyte (see details in the Experimental Section).[19] *p*MA can self-assemble through strong Au–S interactions on the Au surfaces, and is therefore commonly used in the SERS evaluation of Au nanostructures. The characteristic scattering peaks of *p*MA can be clearly observed for all three types of Au NC superstructures at excitation wavelengths of both 633 nm and 785 nm (Figure 4a,b and Figures S7–S10. SERS enhancement factor for of all the 2D and 3D superstructures are calculated; see details in Part SIV in the Supporting Information). The enhancement factors of RD, octahedral, and cubic NC superstructures that have similar numbers of layers (typically 4–6 layers) are 1.0×10^7, 0.8×10^7, and 0.7×10^7, respectively, and the SERS effect of RD superstructures is the strongest among those signals. Given that the multilayered superstructures adsorb similar amounts of *p*MA molecules, it can be concluded that the influence of the electromagnetic field is the main factor for the SERS enhancement. Compared with the multilayers of cubic and octahedral NCs (Figure S4 and S5 in the Supporting Information), the RD NCs in the superstructures more easily form long-range ordered arrangements and well-defined profiles (Figure 1). Therefore, the antenna effect is stronger and more hotspots are generated, thus resulting in the higher SERS intensity in the RD NC superstructures,[20,21] which are therefore better SERS substrates as these NCs form multilayered superstructures at much lower concentrations (0.5 nM).

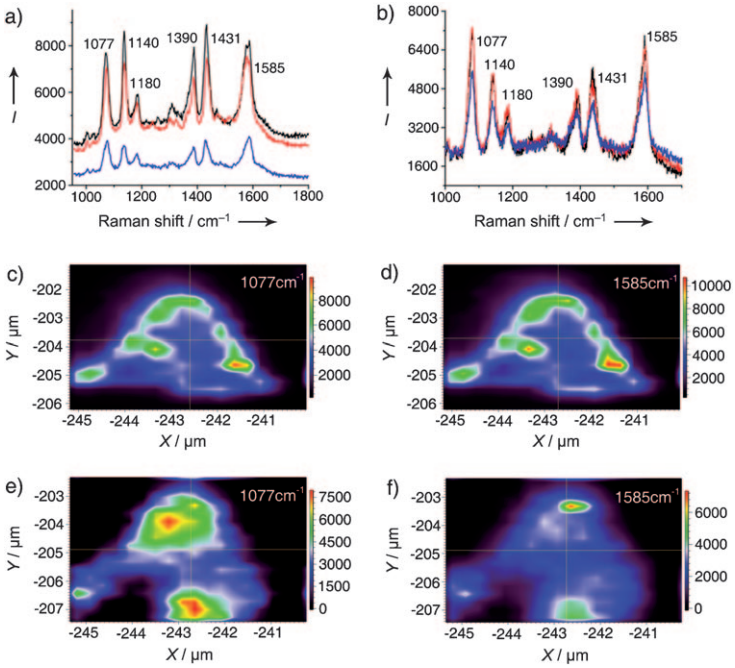

Figure 4. SERS spectra and corresponding mappings of superstructures assembled from RD Au NCs. a) SERS spectra of *p*MA at different locations in RD NC superstructures (excitation with 633 nm laser); b) SERS spectra of *p*MA at different locations in RD NC superstructures (excitation with 785 nm laser; corner: black, edge: red, center: blue); c,d) SERS mappings obtained at the characteristic Raman shift of *p*MA under excitation with 633 nm laser; e,f) SERS mappings obtained at the characteristic Raman shift of *p*MA under excitation with 785 nm laser. The assignments of the peak positions for *p*MA in (a) and (b) are given in Table S2 (see the Supporting Information).

Furthermore, the SERS effects in each type of NC superstructure are quite distinct. Both SERS spectra (Figure 4a,b) and the corresponding mapping (Figure 4c–f) of RD NC superstructures show unique and strong anisotropy, and the Raman scattering intensities at the corners and edges are clearly higher than those in the center. For example, the SERS intensities of both the corners and the edges are around 2.0 times higher than those of the central part under excitation at 633 nm (Figure 4a), while the difference of the SERS intensities is about 1.4 times under excitation at 785 nm (Figure 4b). In contrast, the SERS effect is homogenously distributed in both 2D and 3D superstructures of cubic and octahedral Au NCs, and their spatial anisotropy is not clearly discerned (Figures S7–S10 in the Supporting Information).

To investigate why the triangular superstructures of RD NCs exhibit this unique SERS effect and reveal the origin of anisotropy in the SERS effect, dark-field scattering spectra of NC superstructures were recorded (Figure S11 in the Supporting Information). The optical scattering at the corners and edges in the 3D multilayers of RD NCs for the broad region of 500–900 nm is remarkably stronger than in the central parts, whereas the scattering spectra are identical at different positions for both 2D superstructures of cubic and octahedral NCs. The strong optical scattering at the corners and edges of the triangular multilayer of RD NCs mainly results from significant electromagnetic amplification at these positions, which has been explored as the antenna effect in

previous studies on both individual NCs and NC assemblies.[20–23] However, 2D and 3D superstructures of cubic and octahedral NCs do not have well-defined contours, so the spatial anisotropy is not evident. Quantitatively, the intensities of the optical scattering of both the corners and the edges in the RD NC superstructures is around 1.7 times and 1.5 times higher than those of the central parts at 633 nm and 785 nm, respectively (Figure S11 in the Supporting Information; dotted lines), which correspond to the anisotropic enhancement factors of the SERS signals. This observation is consistent with the fact that the SERS effect in the NC superstructures mainly originates from inelastic scattering of photons among the Au NC units.

In conclusion, monodispersed Au NCs self-assemble into 2D or 3D superstructures, the structure and morphology of which are dependent on the NC shapes. The self-assembly mechanisms have been investigated in detail. Among the different types of 2D or 3D Au NC superstructures, the 3D triangular multilayer exhibits high SERS sensitivity as it has more hotspots and a stronger antenna effect. Furthermore, the SERS intensities at the corners and edges are larger than those in the center of superstructures. The spatial anisotropy is ascribed to strong optical scattering at the corners and edges of the NC superstructures. This work paves the way for the large-scale fabrication of geometrically controllable NC superstructures by rationalizing the interactions between the building blocks, and these designed nanostructures with unique optical properties have many potential applications in the field of chemical or biological sensors and imaging.[13]

Experimental Section

Single-crystalline Au NCs with different shapes were synthesized through a two-step seed-mediated growth by following a previously reported procedure[14] with minor modifications. Cetyltrimethylammonium bromide (CTAB)-capped Au seeds, *N*-hexadecylpyridinium chloride (CPC)-capped Au seeds, CTAB-capped Au nanorods, and RD Au nanocrystals were prepared according to previously reported procedures.[14,24] Octahedral and cubic Au NCs were synthesized under the conditions summarized in Table S1 (see the Supporting Information). The synthesis of the three types of polyhedral Au NCs was terminated by centrifugation (8000 rpm, 5 min); the upper solution was removed and the sample was re-dispersed in 10 mM CPC solution for storage.

2D arrays and 3D superstructures of the Au NCs at different concentrations were formed by the vertical deposition method[15] on Si(111) wafers, Si(100) wafers, or glass cover slides at 60 °C and 80 % humidity. This technique was the same by which photonic crystals were formed through self-assembly of colloidal particles.[16,17] To realize the self-assembly of the nanocrystals, a solution of CPC-capped Au NCs was injected into a 96-pore tissue culture plate with the substrates inserted vertically into each pore. The plates were left in a climatic chamber until the solution evaporated completely. The drying process took about 40 h. Different concentrations of CPC solutions ranging from 1 mM to 100 mM were used, and 10 mM was found to be the optimal concentration. At least 5 parallel samples were employed for each batch, and repetitive experiments were conducted. All substrates were cut into the same size and shape to maintain the conformity of all the experiments.

SERS was carried out with Renishaw inVia microscope. A HeNe laser (633 nm) and a diode laser (785 nm) were used as the light source for the excitation. A solution of *p*MA in ethanol (1.76×10^{-4} M) was dropped onto the superstructures on substrates.

Dark-field scattering spectra were obtained with the combination of white light and a dark-field condenser lens in a Leica microscope in a confocal Raman spectroscope system (Renishaw inVia) through an objective 50× with the numerical aperture of 0.75, which was the same objective for the SERS detection.[25]

AFM characterization was conducted on an atomic force microscope in the tapping mode (SPA 300). Dynamic light scattering (DLS) measurements for size and zeta-potential detection were obtained with a Malvern NanoZS. SEM measurements were performed on a Hitachi S4800 scanning electron microscope at 10.0 kV.

Received: September 2, 2010
Revised: November 16, 2010
Published online: January 5, 2011

Keywords: gold · nanostructures · self-assembly · superstructures · Raman spectroscopy

[1] M. P. Pileni, *Langmuir* **1997**, *13*, 3266 – 3276.
[2] A. I. Hochbaum, R. Fan, R. He, P. Yang, *Nano Lett.* **2005**, *5*, 457 – 460.
[3] E. V. Shevchenko, D. V. Talapin, N. A. Kotov, S. O'Brien, C. B. Murray, *Nature* **2006**, *439*, 55 – 59.
[4] E. V. Shevchenko, D. V. Talapin, C. B. Murray, S. O'Brien, *J. Am. Chem. Soc.* **2006**, *128*, 3620 – 3637.
[5] F. G. Aliev, M. A. Correa-Duarte, A. Mamedov, J. W. Ostrander, M. Giersig, L. M. Liz-Marzan, N. A. Kotov, *Adv. Mater.* **1999**, *11*, 1006 – 1010.
[6] J. A. Schuller, E. S. Barnard, W. Cai, Y. C. Jun, J. S. White, M. L. Brongersma, *Nat. Mater.* **2010**, *9*, 193 – 204.
[7] S. A. Maier, P. G. Kik, H. A. Atwater, S. Meltzer, E. Harel, B. E. Koel, A. A. G. Requicha, *Nat. Mater.* **2003**, *2*, 229 – 232.
[8] N. Fang, H. Lee, C. Sun, X. Zhang, *Science* **2005**, *308*, 534 – 537.
[9] G. Konstantatos, E. H. Sargent, *Nat. Nanotechnol.* **2010**, *5*, 391 – 400.
[10] D. L. Jeanmaire, R. P. Van Duyne, *J. Electroanal. Chem.* **1977**, *84*, 1 – 20.
[11] S. Nie, S. R. Emory, *Science* **1997**, *275*, 1102 – 1106.
[12] P. J. Schuck, D. P. Fromm, A. Sundaramurthy, G. S. Kino, W. E. Moerner, *Phys. Rev. Lett.* **2005**, *94*, 017402.
[13] Z. Tang, S. Liu, *J. Mater. Chem.* **2010**, *20*, 24 – 35.
[14] W. Niu, S. Zheng, D. Wang, X. Liu, H. Li, S. Han, J. Chen, Z. Tang, G. Xu, *J. Am. Chem. Soc.* **2009**, *131*, 697 – 703.
[15] F. Marlow, Muldarisnur, P. Sharifi, R. Brinkmann, C. Mendive, *Angew. Chem.* **2009**, *121*, 6328 – 6351; *Angew. Chem. Int. Ed.* **2009**, *48*, 6212 – 6233.
[16] P. Jiang, J. F. Bertone, K. S. Hwang, V. L. Colvin, *Chem. Mater.* **1999**, *11*, 2132 – 2140.
[17] P. Jiang, K. S. Hwang, D. M. Mittleman, J. F. Bertone, V. L. Colvin, *J. Am. Chem. Soc.* **1999**, *121*, 11630 – 11637.
[18] M. R. Jones, R. J. Macfarlane, B. Lee, J. Zhang, K. L. Young, A. J. Senesi, C. A. Mirkin, *Nat. Mater.* **2010**, *9*, 913 – 917.
[19] H. Wang, C. S. Levin, N. J. Halas, *J. Am. Chem. Soc.* **2005**, *127*, 14992 – 14493.
[20] H. Ko, S. Singamaneni, V. V. Tsukruk, *Small* **2008**, *4*, 1576 – 1599.
[21] J. M. McLellan, A. Siekkinen, J. Chen, Y. Xia, *Chen. Phys. Lett.* **2006**, *427*, 122 – 126.
[22] J. A. Dieringer, K. L. Wustholz, D. J. Masiello, J. P. Camden, S. L. Kleinman, G. C. Schatz, R. P. Van Duyne, *J. Am. Chem. Soc.* **2009**, *131*, 849 – 854.
[23] K. L. Wustholz, A. I. Henry, J. M. McMahon, R. G. Freeman, N. Valley, M. E. Piotti, M. J. Natan, G. C. Schatz, R. P. Van Duyne, *J. Am. Chem. Soc.* **2010**, *132*, 10903 – 10910.
[24] T. K. Sau, C. J. Murphy, *Langmuir* **2004**, *20*, 6414 – 6420.
[25] M. K. Hossain, Y. Kitahama, G. G. Huang, T. Kaneko, Y. Ozaki, *Appl. Phys. B* **2008**, *93*, 165 – 170.

